MNRAS **000**, 1–15 (2017) Preprint 20 February 2017 Compiled using MNRAS LATEX style file v3.0

The Nature of the Faint Low-Frequency Radio Source Population

E. F. Ocran[1,2], A. R. Taylor[1,2], M. Vaccari[1,3], D. A. Green[4],
[1] *Department of Physics and Astronomy, University of the Western Cape, Private Bag X17, Bellville 7535, South Africa*
[2] *Department of Astronomy, University of Cape Town, Private Bag X3, Rondebosch 7701, South Africa*
[3] *INAF - Istituto di Radioastronomia, via Gobetti 101, 40129 Bologna, Italy*
[4] *Astrophysics Group, Cavendish Laboratory, Cambridge University, 19 J. J. Thompson Ave., Cambridge, CB3 0HE, UK*

arXiv:1702.04962v2 [astro-ph.GA] 17 Feb 2017

Accepted 2017 February 16. Received 2017 February 15; in original form 2016 December 17

ABSTRACT

We present a multi-wavelength study into the nature of faint radio sources in a deep radio image with the Giant Meterwave Radio Telescope at 612 MHz covering 1.2 deg^2 of the ELAIS N1 region. We detect 2800 sources above 50 μJy beam^{-1}. By matching to multi-wavelength data we obtain a redshift estimate for 63%, with 29% based on spectroscopy. For 1526 of the sources with redshifts we use radio and X-ray luminosity, optical spectroscopy, mid-infrared colors, and 24μm and IR to radio flux ratios to search for the presence of an AGN. The analysis reveals a rapid change in the population as flux density decreases from ∼500 μJy to ∼100 μJy. We find that 80.3% of the objects show no evidence of AGN and have multi-wavelength properties consistent with radio emission from star forming galaxies (SFG). We classify 11.4% as Radio Quiet (RQ) AGN and the remaining 8.3% as Radio Loud (RL) AGN.

The redshift of all populations extends to $z > 3$ with a median of ∼1. The median radio and far-IR luminosity increases systematically from SFG, to RQ AGN and RL AGN. The median $q_{24\mu m}$ for SFG, 0.89 ± 0.01 is slightly below that for RQ AGN, 1.05 ± 0.03, and both differ substantially from the value for RL AGN of -0.06 ± 0.07. However, SFG and RQ AGN show no significant difference in far-IR/radio ratios and have statistically indistinguishable star formation rates inferred from radio and far-IR luminosities. We conclude that radio emission from host galaxies of RQ AGN in this flux density regime result primarily from star formation activity.

Key words: galaxies: active, infrared: galaxies, radio continuum: galaxies

1 INTRODUCTION

The interplay between star formation and black hole accretion is one of the central issues in galaxy evolution today. Tight correlations found between black hole mass and both stellar bulge mass (Kormendy et al. 1998; McLure & Dunlop 2002) and velocity dispersion (Gebhardt et al. 2000; Tremaine et al. 2002) in galaxies in the local universe indicates that the formation and growth of galaxies is closely linked to the growth of their central black holes.

Both accretion activity on the central black holes and star formation in the disks of galaxies create radio synchrotron emission. In this context, the study of the faint radio universe has become a very active field of research as the increased sensitivity of radio telescopes has enabled μJy-rms-level imaging over extended fields (Luchsinger et al. 2015), probing radio emission from galaxies to significant red shift. Understanding the properties of sources in the faint radio sky and their cosmic evolution is thus important to understanding of the links between black hole accretion and star formation activity in the universe (Casey et al. 2009).

Whereas the bright (i.e. > 1 mJy at 1.4 GHz) radio sky is dominated by the emission driven by 'radio-loud' AGNs (RL AGN) (e.g. Prandoni et al. 2001; Seymour et al. 2008; Padovani et al. 2009), deep radio surveys probe both active galactic nuclei (AGN) and star-forming galaxies (SFG), with SFGs becoming increasingly important at fainter flux densities. Recent work by Padovani et al. (2009) and Bonzini et al. (2013) has revealed a third population of sources at faint flux densities, the 'radio-quiet' AGN (RQ AGN). Giroletti & Panessa (2009) proposed that RQ AGN represent scaled-down versions of RL AGN in mini radio jets. On the other hand, Kimball et al. (2011) and Padovani et al. (2011) argued that the radio emission of RQ AGN come from star formation in the host galaxy.

Radio flux density measurements at angular resolutions insufficient to resolve the structure of the galaxy cannot distinguish between synchrotron emission from AGN or star

© 2017 The Authors

formation. However, multi-wavelength observations from the X-ray to the millimetre can reveal the presence of AGN, including highly obscured ones. Rawlings et al. (2015) divided faint radio samples into sources powered by AGN or by star formation through their infrared SEDs, X-ray luminosities and IRAC colors satisfying the Donley et al. (2012) criterion. Bonzini et al. (2013) proposed a classification scheme which is an upgrade of that used by Padovani et al. (2011) through a combination of radio, infrared and X-ray data in the ECDFS.

In this work, we present a multi-wavelength investigation to classify radio sources from deep 612 MHz observations with the GMRT of the ELAIS N1 field covering an area of 1.2 deg^2 to a RMS sensitivity of 10 μJy beam^{-1}. These observations are the most sensitive images of the sky at this frequency to date. Garn et al. (2008) presented a GMRT image of ELAIS N1 at 610 MHz covering ∼9 deg^2, constructed from a mosaic of 19 pointings. This comprised a smaller central region of 4 pointings with an rms of ∼40 μJy beam^{-1} and the remaining 15 pointings with an rms of ∼70 μJy beam^{-1}. Grant et al. (2010) imaged 15 deg^2 at 1.4 GHz with the Dominion Radio Astrophysical Observatory to an rms of 55 μJy beam^{-1} in total intensity and 45 μJy beam^{-1} in linear polarization. While stacking analysis of such deep radio images based on optical-IR catalogues has allowed statistical correlations such as the average radio-IR correlation to be explored to lower radio flux densities (Garn & Alexander 2009), direct studies of the radio selected population to μJy sensitives, ultra-deep radio imaging.

The paper is organized as follows. We describe the radio observations and the multi-wavelength data and sample selection in Section 2. The multi-wavelength AGN diagnostics are described in Section 5, and the properties of the classified sources in Section 6. We summarize our results in Section 7. For calculation of intrinsic source properties we assume a flat cold dark matter (ΛCDM) cosmology with $\Omega_\Lambda = 0.7$, $\Omega_m = 0.3$ and $H_o = 70$ km s^{-1} Mpc^{-1} .

2 MULTI-WAVELENGTH DATA

2.1 Radio Data

GMRT observations of the ELAIS N1 field were obtained during several observing runs from 2011 to 2013. Observations were carried out for 7 positions arranged in a hexagonal pattern centred on $\alpha = 16^h\ 10^m\ 30^s$, $\delta = 54°\ 35\ 00''$, covering an area of 1.2 deg^2. Each position was observed for ∼30 hours in three 10-hour sessions. The total bandwidth was 32 MHz, split into 256 spectral channels centered at 612 MHz in four polarization states. Observations of 3C286 were made twice in each observing session, and were used to calibrate the flux scale, band pass and absolute polarization position angle. Time dependent gains and on-axis polarisation leakage corrections were measured by frequent observations of the secondary calibrator J1549+506.

The visibility data were calibrated, imaged and mosaicked using the CASA processing software. Images were constructed for each pointing out to the 10% point of the primary beam using multi-frequency synthesis with two Taylor series terms. The effect of the 3-dimensional beam over the wide field-of-view was corrected using w-projection. Following initial calibration, the visibilities for each pointing were run through several iterations of self-calibration, with the gain solution time interval decreasing and the depth of the clean component sky model increasing with each iteration. The self-calibrated individual field images were combined into a mosaic in the image plane using the CASA linearmosaic tool. The RMS noise in the resulting total intensity mosaic image is 10.3 μJy beam^{-1} before primary beam correction. The RMS was measured by fitting a normal error function to distribution of negative map deflections from the entire mosaic. By comparison, the RMS in the Stokes Q and U images is 7.3 μJy beam^{-1}. The RMS noise in the total intensity mosaic is thus only slightly above the thermal noise limit. The excess noise may be attributed to a combination of confusion and residual clean artifacts.

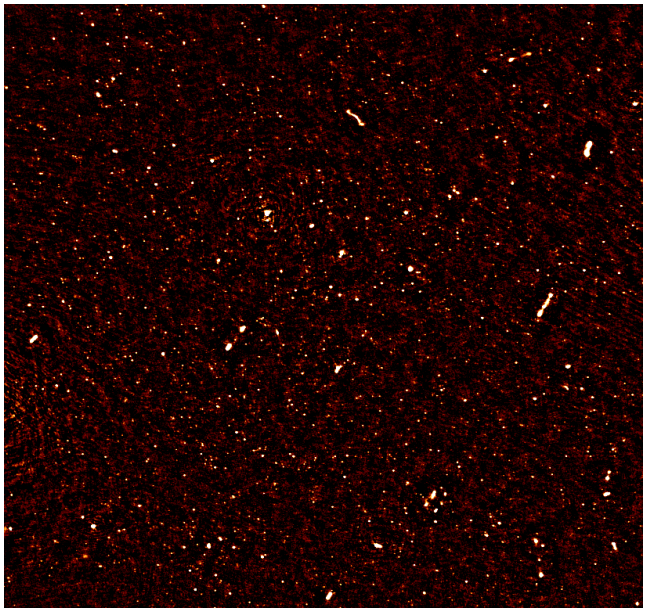

Figure 1. Image of the ELAIS N1 GMRT 612 MHz mosaic centered at $\alpha = 16^h\ 10^m\ 30^s$, $\delta = 54°\ 35\ 00''$. This image is 47′ on each side, showing the central ∼0.6 deg^2 of the 1.2 deg^2 mosaic. The RMS noise is 10.3 μJy beam^{-1}. The image shows a small number of bright classical radio galaxies with double-lobed and jet morphologies. However, the vast majority of the radio sources are fainter objects that are unresolved at the ∼ 5″ angular resolution.

The angular resolution of the mosaic radio image is 6.1× 5.1 arcsec. An image of the central 0.6 deg^2 of the mosaic is shown in Figure 1.

The catalogue of radio sources was extracted using the AIPS SAD automated source finding program and consists of 2800 radio sources with peak flux density above the 5σ threshold. Among the brightest objects in the sample, is the very small fraction of the total (∼3%) that exhibit classical extended radio-galaxy, AGN-driven jet morphology (Taylor & Jagannathan 2016). The vast majority are compact sources that are unresolved at the resolution of the observations. The flux densities for compact individual sources was derived from the 2-D Gaussian fits from AIPS SAD. Total flux densities for the small number of extended multicomponent jet-lobe sources was taken to be the sum of the flux densities of the individual components. The full catalogue, including source counts and polarization information,

will be published in a subsequent paper. Here we focus on matching with the multi-wavelength data sets to investigate the nature of the radio sources.

2.2 SERVS Data Fusion and Ancillary Data

The Spitzer Extragalactic Representative Volume Survey (SERVS, Mauduit et al. 2012) is a warm Spitzer survey which imaged 18 deg^2 using the IRAC1 3.6 μm and IRAC2 4.5 μm bands. The main aim of the survey was to enable the study of galaxy evolution as a function of environment from z ∼ 5 to the present day through the first extragalactic survey that is both large enough and deep enough to put rare objects such as luminous quasars and galaxy clusters at $z \geq 1$ into their cosmological context. SERVS sources were separately extracted in IRAC1 and IRAC2 images and single-band detections were merged into a two-band (hereafter IRAC12) catalogue using a search radius of 1 arcsec. The rms noise of both the IRAC1 and IRAC2 images is 0.5 μJy and the catalogue completeness limit is thus 2 μJy in both bands.

SERVS overlaps with several other surveys at optical, near- through far-infrared, sub-millimeter. The SERVS Data Fusion[1] (Vaccari et al. 2010; Vaccari 2015), matches SERVS IRAC12 sources against a large suite of multi-wavelength data using a search radius of 1 arcsec. In particular, in our work we have used the following datasets included within the SERVS Data Fusion:

- SDSS DR12 Optical Photometry (Alam et al. 2015)
- INT WFC Deep Optical Photometry (González-Solares et al. 2011)
- 2MASS PSC Near-IR Photometry (Cutri et al. 2003)
- UKIDSS DXS Deep Near-IR Photometry (Lawrence et al. 2007)
- Spitzer Wide-Area Infrared Survey 4-band IRAC Photometry and 3-band MIPS Photometry (Lonsdale et al. 2003; Vaccari 2015)
- SWIRE Photometric Redshifts (Rowan-Robinson et al. 2008, 2013, 2016)
- Spectroscopic redshifts from the literature (Serjeant et al. 2004; Trichas et al. 2009; Hernán-Caballero et al. 2009; Alam et al. 2015) including newly obtained measurements from BOSS/SDSS-III better detailed in Sec. 2.3

In future papers, we will improve our analysis by making use of the multi-wavelength database produced by the Herschel Extragalactic Legacy Project (Vaccari 2016, HELP), including an improved source extraction at SPIRE Griffin et al. (2010) wavelengths using the XID+ software by Hurley et al. (2017).

2.3 BOSS/SDSS Spectroscopy

The Baryon Oscillation Spectroscopic Survey (BOSS) was the primary dark-time survey of SDSS-III Eisenstein et al. (2011), the third phase of the Sloan Digital Sky Survey (SDSS, York et al. 2000). BOSS observed 1.5 million massive galaxies and 150,000 quasars to measure the distance-redshift relation $d_A(z)$ and the Hubble parameter $H(z)$ with percent-level precision out to $z = 0.7$ and $z \simeq 2.5$, using the well-established techniques that led to the first detection of the baryon acoustic oscillations (BAO) feature (Cole et al. 2005; Eisenstein et al. 2005). BOSS was designed to measure the scale of the BAO in the clustering of matter over a larger volume than the combined efforts of all previous spectroscopic surveys of large-scale structure. BOSS consists of two spectroscopic surveys, both of which have been carried out over an area of 10,000 deg^2. The first survey observed 1.5 million luminous red galaxies ($i < 19.9$) to measure BAO to redshifts $z < 0.7$, while the second one will observe neutral hydrogen in the Lyα forest in more than 150,000 quasar spectra ($g < 22$) to constrain BAO at $z \sim 2.5$.

From 2012 onwards, a series of plates were added to the SDSS-III program to observe ancillary science programs. We were granted four BOSS plates to obtain spectra for the radio sources detected by our GMRT observations as well as by other shallower radio surveys in the ELAIS N1 field. Observations were obtained by the SDSS team and their reduction using the default BOSS spectroscopic pipeline has been made publicly available as part of the SDSS DR12. In our work, however, due to the large number of sources near the center of the BOSS plate, a bespoke data reduction scheme was adopted to optimize the spectroscopic redshift accuracy (Tarr et. al. in prep).

2.4 X-Ray Data

The only astrophysical sources that reach very high X-ray luminosities are AGNs. Usually a cut in the unabsorbed X-ray luminosity at 10^{42} erg s^{-1} is considered as a threshold dividing AGNs and SFGs (see Szokoly et al. 2004). In this work we combined shallow Chandra observations of the whole GMRT field produced by Trichas et al. (2009) using the Imperial College London pipeline (Georgakakis et al. 2008; Laird et al. 2009) with deep Chandra observations of a small area (0.15 deg^2) of the central region of the field by Manners et al. (2003).

3 MULTI-WAVELENGTH CROSS-MATCHING

We matched the GMRT catalogue against SERVS IRAC12 positions using a variable search radius equal to three times the estimated astrometric error. Radio position errors for individual sources from AIPS SAD fitting algorithm are typically a few a tenths of an arcsecond. SERVS astrometric error of 0.15 arcsec was assumed based on SERVS vs 2MASS cross-matching. From an initial matching of the GMRT and SERVS catalogues we computed the median astrometric offsets between the two catalogues of −0.434±0.014 and +0.303 ± 0.013 arcsec in RA and DEC respectively. We applied these correction to the radio positions before performing the final cross-matching. SERVS matches were identified using a search radius of three times the combined astrometric error on the coordinate comparison. Given the sub-arcsecond accuracy of the positions,in virtually all cases where a match was found this resulted in a unique identification. In the few cases of a multiple SERVS objects in error circle we took the nearest object as the identification.

SERVS identifications were obtained for 2369 out of

[1] http://www.mattiavaccari.net/df

Table 1. GMRT cross-matching statistics. The table shows statistics from our new cross-matching.

Catalogue	Size	Fraction (%)
GMRT	2800	100%
SERVS band 1 or 2	2369	85%
SERVS band 1 and 2	2234	80%
SWIRE all IRAC bands	1091	39%
MIPS 24 μm	1672	60%
X-RAY	92	3.3%
MRR13-PHOTZ	1456	52%
MRR13-FIR-LUM	1279	46%
SPECZ	817	29%
REDSHIFTS	1760	63%

2800 (or 85%) of our radio sources. The RMS of the coordinate differences for the matched sources is ∼0.5″ in both RA and DEC. Of the 15% of GMRT objects that are not matched in the SERVS catalogue, 203 (7.3%) are affected by diffraction spikes due to bright objects and/or by source blending due to confusion, and therefore no conclusive identifications can be made. This can partly be addressed by carrying out multi-band forced photometry with e.g. the Tractor code (Lang et al. 2016), as currently underway within the SERVS team (Nyland et al. in prep). Another 109 objects (3.9%) have faint counterparts in the SERVS images but have no entry in the SERVS catalogue. The remaining 124 unidentified objects (4.4%) have no infrared counterpart in the SERVS image. These objects are examples of the recently identified class of Infra-red Faint Radio Sources (Norris et al. 2006; Garn & Alexander 2008).

Table 1 summarizes the results of the cross-matching against SERVS and the other multi-wavelength data sets. The fraction of identifications in either SERVS IRAC1 or IRAC2 is 85%, while 80% have counterparts in both IRAC1 and IRAC2 and 39% of our radio sample has counterparts in all four IRAC bands. MIPS 24 detections are found for 60%. In addition, 3.3% of our sample has an X-ray detection in either the shallow or deep X-ray (2.5% and 0.8% respectively).

4 REDSHIFTS

The majority of the spectroscopic redshifts for our sample were obtained with BOSS. The BOSS spectral classification and redshift analyses are based on a χ^2 minimization of linear fits to each observed spectrum using multiple templates (Bolton et al. 2012). The BOSS spectroscopic redshifts were supplemented by a small number of redshifts available from the literature. For sources where a spectroscopic redshift was not available, we use photometric redshift estimates from the revised SWIRE Photometric Redshift Catalogue (Rowan-Robinson et al. 2013). The SWIRE catalogue takes into account new optical photometry in several of the SWIRE areas, and incorporates Two Micron All Sky Survey (2MASS) and UKIRT Infrared Deep Sky Survey (UKIDSS) near-infrared data. It is the most reliable photometric redshift catalogue publicly available in ELAIS N1, and covers the full GMRT mosaic.

The redshift statistics for our sample are summarized in

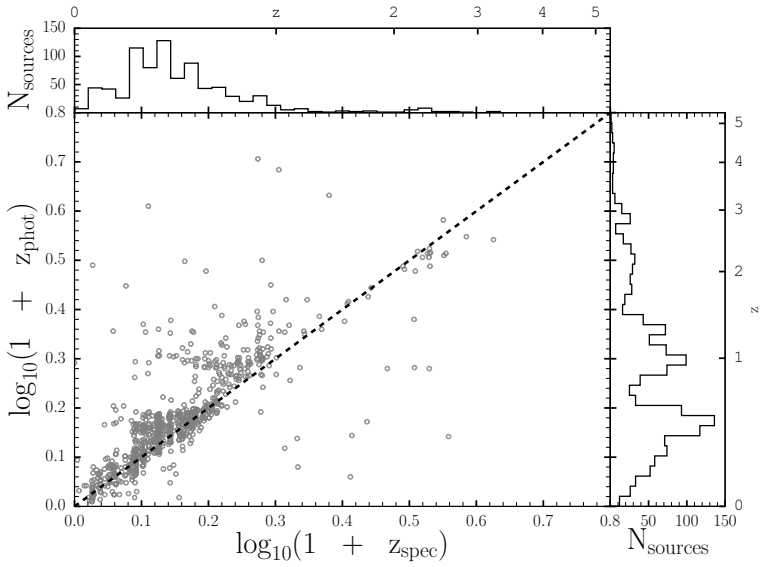

Figure 2. Comparison between photometric and spectroscopic redshift for sources with both. The dashed black line corresponds to $z_{spec} = z_{phot}$. The top and right histograms show spectroscopic and photometric redshifts respectively.

Table 1. Spectroscopic redshifts are available for 29%. The SWIRE catalogue provides photometric redshifts for 52% of our sample and far-infrared luminosities for 46%. Combined 63% of our sample has either a spectroscopic or photometric redshift. Figure 2 compares photometric and spectroscopic redshifts for sources with both. The histograms at the top and on the right-hand side of the figure show the distributions of photometric and spectroscopic redshifts respectively. In general, the two redshifts agree out to spectroscopic redshift $z_{spec} < 1$ (i.e. $\log_{10}(1+z) < 0.3$). However, a non-negligible number of outliers can be seen creating a spurious peak in the photometric redshift distribution at $z_{phot} \sim 1$.

Figure 3 shows the distribution of the difference $(\Delta z)/(1+z_{spec})$, where $\Delta z = z_{phot} - z_{spec}$. The standard deviation of this distribution is $\sigma[\Delta z/(1+z)] \sim 0.20$. Outliers with $|\Delta z|\,/\,1+z_{spec} > 0.2$ make up 10.40% of our sample.

We also compute the normalized median absolute deviation:

$$\sigma_{\rm NMAD} = 1.48 \times {\rm median}\left(\frac{|\Delta z - {\rm median}(\Delta z)|}{1+z_{\rm spec}}\right), \quad (1)$$

an estimate of the quality of photometric redshift which is less sensitive to outliers (Brammer et al. 2008). We find $\sigma_{\rm NMAD} = 0.074$, which is slightly higher than found in other photometric redshift catalogues (e.g. see Ilbert et al. 2009; Taylor et al. 2009; Cardamone et al. 2010).

5 AGN DIAGNOSTICS

Of our total sample of 2800 radio sources, 1760 have either a spectroscopic or a photometric redshift estimate. Out of these, 1526 have at least one multi-wavelength (i.e. not only based on radio properties) AGN diagnostic and constitute our final sample for the purposes of source classification. In

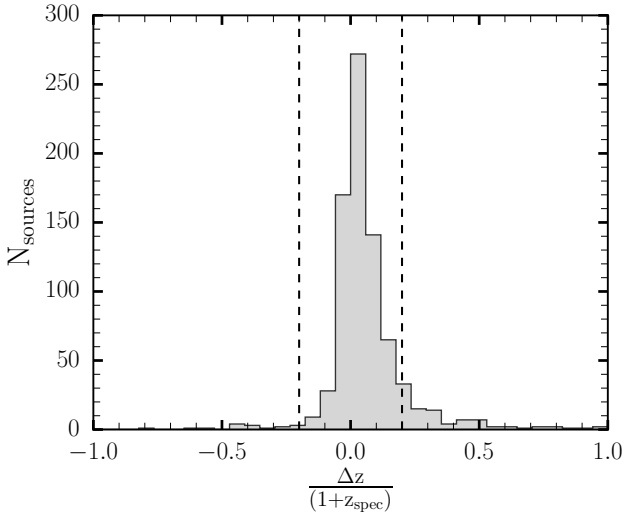

Figure 3. Histogram showing the distribution of the $|\Delta z|/(1 + z_{spec})$ the dash vertical lines indicate $|\Delta z|/(1 + z_{spec}) = 0.2$. The mean ($\mu$) and standard deviation (σ) are 0.07 and 0.20 respectively.

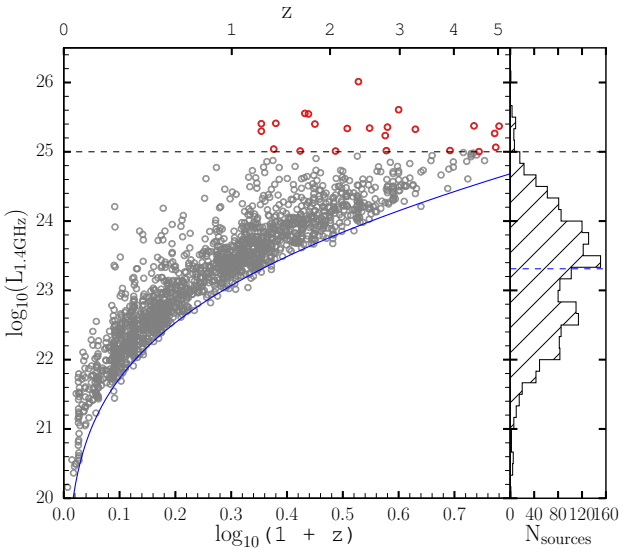

Figure 4. Radio Loud AGN Selection. The plot shows 1.4 GHz luminosity versus redshift for the GMRT sample with redshifts. The dashed black line shows a radio luminosity threshold of 10^{25} W Hz^{-1}. Sources above this luminosity are classified as RL AGN (red circles). The luminosity detection limit implied by the GMRT sensitivity is shown by the solid blue curve. The blue dashed line in the right hand histogram shows the median 1.4 GHz luminosity.

this section we describe the combination of multi-wavelength AGN diagnostics employed to obtain a census of galaxies showing evidence of hosting an AGN within this sample.

5.1 Radio Diagnostics

The first criteria we use to identify AGNs in our radio sample are the radio luminosities. The 612 MHz radio flux densities were converted to rest-frame 1.4 GHz effective luminosities assuming a radio spectral index of $\alpha = -0.7$ (Ibar et al. 2010) as:

$$L_{1.4\,\mathrm{GHz}} = 4\pi d_{\mathrm{lum}}^2 \frac{S_{1.4\,\mathrm{GHz}}}{(1+z)^{1+\alpha}} \quad (2)$$

where

$$S_{1.4\,\mathrm{GHz}} = \left(\frac{1.4}{0.61}\right)^{\alpha} S_{0.6\,\mathrm{GHz}}. \quad (3)$$

We classify sources as RL AGNs based on a radio luminosity cut of $L_{1.4\,\mathrm{GHz}} > 10^{25}$ W Hz^{-1}, as suggested by e.g., Sajina et al. (2007); Jiang et al. (2007) and Sajina et al. (2008) and illustrated by Figure 4. We note that this is a conservative criterion, as it only selects the brightest radio-loud galaxies and quasars. Mauch & Sadler (2007) showed that the AGN radio luminosity function flattens at low luminosities, indicating that there remains a fraction of AGN powered radio sources below the cutoff. Our radio luminosity selection criterion, identifies 26 RL AGN sources, constituting 1.5% of the population with redshifts.

5.2 X-ray Diagnostics

X-ray surveys are perhaps one of the most reliable methods to select AGNs, since they directly probe their high energy emission. However dusty tori may obscure the X-ray emission and reprocess it into infrared emission. Thus, AGN detections through X-ray and infrared are largely complementary (Fadda & Rodighiero 2014). We computed the hard X-ray luminosity (2 -10 keV) using the relation

$$L_{\mathrm{x}} = 4\pi S_{\mathrm{x}} d_{\mathrm{L}}^2 (1+z)^{2-\gamma}. \quad (4)$$

where we fixed the photon-index to the commonly observed value of $\gamma = 1.8$ (Dadina 2008; Vito et al. 2014). Figure 5 shows the x-ray luminosity for the 70 objects having redshifts that are detected in either the x-ray deep or x-ray shallow datasets. This includes only 1 of the 26 sources classified as RL AGN in the previous section. We classify a source as an AGN based on x-ray emission when $L_{\mathrm{x}} > 10^{42}$ erg s^{-1} following e.g. Szokoly et al. (2004). All but one source of the 70 objects lies above this threshold. We therefore classify 69 sources as hosting AGNs through this X-ray criterion, representing 4.0% of our radio sample with redshifts.

5.3 BOSS/SDSS Diagnostics

From our cross-matching, we were able to associate 779 of the GMRT sources with BOSS spectroscopic redshifts and classifications. The BOSS CLASS and SUBCLASS parameters, as detailed by Bolton et al. (2012), classify spectra as:

1. GALAXY: identified with a galaxy template and can have the following subclasses:

   a. STARFORMING: the spectrum has detectable emission lines that are consistent with star formation accord-

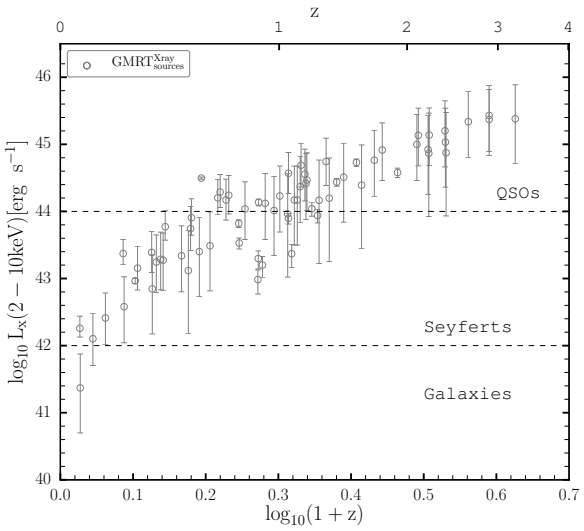

Figure 5. X-ray luminosity as a function of redshift for the GMRT sources with X-ray detections. The dash horizontal line represents the typical demarcations for Galaxies, Seyferts and QSOs.

ing to the criterion:

$\log_{10}(\mathrm{OIII/H}\beta) < 0.7 - 1.2(\log_{10}(\mathrm{NII/H}\alpha) + 0.4)$

b. STARBURST: galaxy is star-forming with an equivalent width of Hα greater than 50 Å

c. AGN: the spectrum has detectable emission lines that are consistent with being a Seyfert or a LINER:

$\log_{10}(\mathrm{OIII/H}\beta) > 0.7 - 1.2(\log_{10}(\mathrm{NII/H}\alpha) + 0.4)$

2. QSO: identified with a QSO template.

3. STAR: identified with a stellar template.

In addition, any galaxies or quasars that have lines detected at the 10σ level with velocity dispersion > 200 km s^{-1} at the 5σ level, have the category BROADLINE appended to their SUBCLASS.

The BOSS analysis of the 779 sources yields 703 GALAXY and 73 QSO classifications. The remaining 3 sources were identified as STARS. Among the 703 GALAXY CLASS, 19 are classified as SUBCLASS AGN. Conversely, 172 sources are classified as STARFORMING and 141 classified as STARBURST. Four sources are classified are STARBURST BROADLINE and 43 sources classified as BROADLINE. The remaining 324 sources of the 703 GALAXY class had no SUBCLASS associations.

Of the three BOSS spectra identified as STARS their SUBCLASS parameter indicates that they are an M4.5:111, GOVa, and a cataclysmic variable star respectively. We do not include these sources in our BOSS selection.

We classify as AGN all objects with a BOSS QSO class, as well as any source having a BOSS GALAXY class with a SUBCLASS parameter of either AGN, BROADLINE or STARBURST BROADLINE. All others GALAXY class are taken to be SFG. Table 2 presents the breakdown of the number of the SFGs and AGNs from the BOSS spectroscopic classifications.

Table 2. BOSS spectroscopic classifications results.

Category	Number	Fraction
SFG	683	39.7%
AGN	96	5.5%

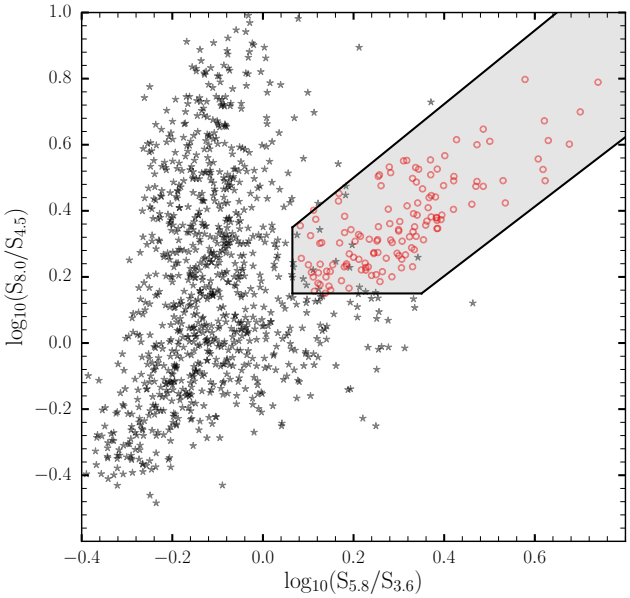

Figure 6. IRAC color-color diagram showing the separation between AGNs (open red circles) and SFGs (black stars). The shaded region indicates the area within the Donely wedge.

5.4 IRAC Color Diagnostics

The IRAC four-band color-color plane was used to identify AGNs adopting the criterion proposed by Donley et al. (2012) and defined as:

$$x = \log_{10}\left(\frac{f_{5.8\mu m}}{f_{3.6\mu m}}\right), \quad y = \log_{10}\left(\frac{f_{8.0\mu m}}{f_{4.5\mu m}}\right) \tag{5}$$

$$\begin{aligned} & x \geq 0.08 \ \wedge \ y \geq 0.15 \\ & \wedge y \geq (1.21 \times x) - 0.27 \\ & \wedge y \leq (1.21 \times x) + 0.27 \\ & \wedge f_{4.5\mu m} > f_{3.6\mu m} > f_{4.5\mu m} \wedge f_{8.0\mu m} > f_{5.8\mu m} \end{aligned} \tag{6}$$

This criterion have been designed to reject the majority of low and high redshift star-forming contaminants in the Lacy et al. (2004, 2007) and Stern et al. (2005) AGN selection wedges. Figure 6 presents IRAC color-color diagram for our 1091 GMRT sources with four IRAC band detections. We select 138 sources from this criterion. Of these, 123 sources have redshift estimates, constituting 7.0% of the radio sources with redshift.

5.5 Mid-Infrared - Radio Flux Ratio

The MIPS (Rieke et al. 2004) 24μm flux density and the effective 1.4 GHz flux density, $S_{1.4\,\mathrm{GHz}}$ (Equation 3), were used to calculate the $q_{24\mu\mathrm{m}}$ parameter,

$$q_{24\mu\mathrm{m}} = \log_{10}(S_{24\mu\mathrm{m}}/S_{1.4\,\mathrm{GHz}}). \quad (7)$$

We compute $q_{24\mu\mathrm{m}}$ for the radio sources with MIPS 24μm detections and redshifts and compare it to the redshifted $q_{24\mu\mathrm{m}}$ value for the M82 local standard starburst galaxy template as done by Bonzini et al. (2013) to identify SFGs and radio-loud AGNs. We normalize the M82 SED to the local average value of $q_{24\mu\mathrm{m}}$ obtained by Sargent et al. (2010) and define the SFG locus as the region within $\pm 2\sigma$ of the normalized M82 template in the $(q_{24\mu\mathrm{m}}, z)$ plane, where σ is the 0.35 average spread for local sources by Sargent et al. (2010). Sources below this locus display a radio excess with respect to SFGs and are therefore classified as Radio-Loud AGNs.

The results for our sources are illustrated in the top panel of Figure 7. The black stars, open red squares above the $-2\,\sigma$ dispersion curve (dash black curve) represents the SFGs and RQ AGN respectively. This criterion, initially selects 42 radio sources as RL AGN (open red circles in Figure 7) constituting $\sim$ 2.4% of the radio population with redshifts. We compare this method to the radio-loud AGN classification based on radio luminosity in Section 5.1. Of the 26 sources selected as radio-loud AGNs according to their radio luminosity 15 have mid-infrared detections. Amongst these, only 5 are also classified as radio-loud using the $q_{24\mu\mathrm{m}}$ selection criterion. For the sources with a redshift detection but no MIPS counterpart, we assumed that:

$$S_{24\mu\mathrm{m}} < S_{24\mu\mathrm{m\,lim}} = 286.6\mu\,Jy \quad (8)$$

and thus the upper limit (downward pointing arrow symbols in Figure 7 is given by:

$$q_{24\mu\mathrm{m\,lim}} = \log_{10}(S_{24\mu\mathrm{m\,lim}}/S_{1.4\,\mathrm{GHz}}) \quad (9)$$

For our sources with redshifts within the same range studied by Sargent et al. (2010), **i.e** $z \sim 1.4$, we measure a median $q_{24\mu\mathrm{m}}$ value of 1.10±0.02, whereas for our full sample with redshifts we measure a median $q_{24\mu\mathrm{m}} = 0.86 \pm 0.01$ at a median redshift of $\sim$ 0.71. We estimated the median and the error on the median using the median absolute deviation estimator as this is a more robust measure of the variability of a univariate sample of quantitative data than the standard deviation (Rousseeuw & Croux 1993). Our result is in agreement with and more precise than previous work from Appleton et al. (2004) who estimated $q_{24\mu\mathrm{m}} = 0.84 \pm 0.28$ by matching over 500 Spitzer sources at 24μm with VLA 1.4 GHz μJy radio sources for the Spitzer First Look Survey (FLS) extending to $z > 2$. Huynh et al. (2010) measured a median $q_{24\mu\mathrm{m}} = 0.71 \pm 0.31$ for 84 sources with detections in both the IR and radio for observations of the Hubble Deep Field South taken with the Spitzer Space Telescope up to $z > 1$.

5.6 AGN/SFG Classification Overview

We have carried out a multi-wavelength study using optical, X-ray, infrared and radio data to search for evidence of the presence of an AGN in our sample of 1526 radio sources using five criteria:

(i) Radio power, $L_{1.4\,\mathrm{GHz}} \geq 10^{25}$ W Hz^{-1}.
(ii) X-ray luminosity, $L_{\mathrm{x}} \geq 10^{42}$ erg s^{-1}.
(iii) BOSS AGN spectroscopic classification.
(iv) IRAC colors using the Donley et al. (2012) criteria.
(v) Mid-Infrared to radio flux ratio using the Bonzini et al. (2013) criterion.

The 612-MHz flux density distribution of the sample is shown in Figure 8. The entire range of flux densities in the total GMRT population is sampled. The minimum flux density for the 1526 sources with AGN diagnostics is 52 μJy and the median flux density is 123.3 μJy, close to the median of 128.8 μJy for the total sample.

Combining all the indicators we identify sources that exhibit evidence of the presence of an AGN. The break-

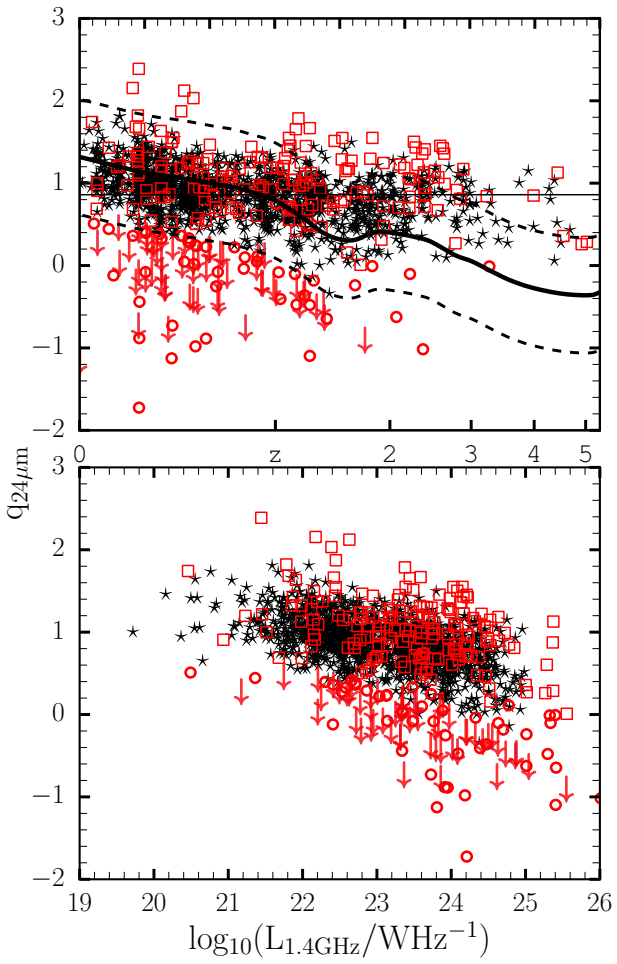

Figure 7. Top: $q_{24\mu\mathrm{m}}$, the logarithm of the ratio between the mid-infrared and radio flux for the GMRT sources with redshift estimates. The solid black curve shows the predicted value of M82 template, the dividing line between radio-quiet and radio-loud AGNs with $\pm 2\sigma$ dispersion (dash black curve). The horizontal line is the median value of $q_{24\mu\mathrm{m}}$ for the sources. The black stars, open red squares and open red circles SFGs, RQ AGN and RL AGN respectively. The downward pointing arrows represent RL AGN with upper limits (see Equation 9)). Bottom: 24μm vs. 1.4 GHz luminosity for SFGs, RQ AGNs and RL AGNs.

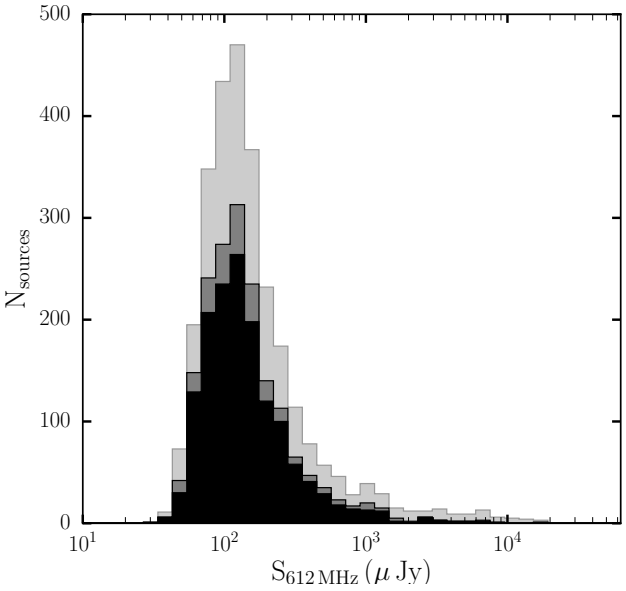

Figure 8. The distribution of 612-MHz flux densities for the entire GMRT sample of 2800 sources (light gray), radio sources with redshifts (dark gray) and sources with redshifts that also have at least one diagnostic for AGN activity (black).

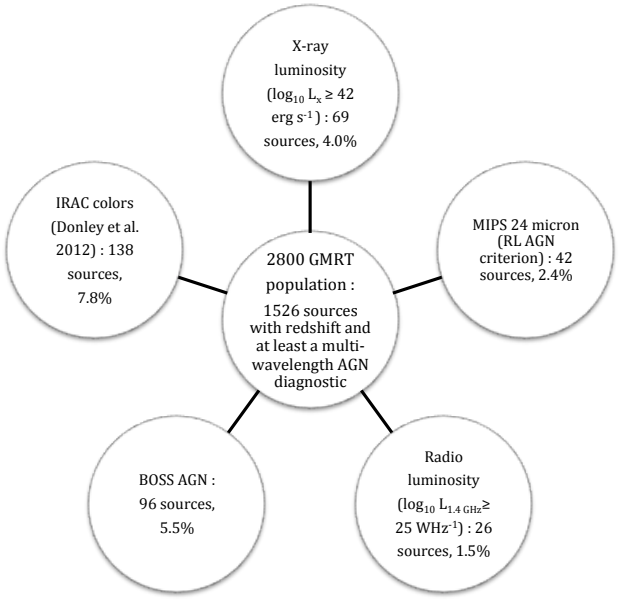
X-ray luminosity ($\log_{10} L_x \geq 42$ erg s^{-1}) : 69 sources, 4.0%
IRAC colors (Donley et al. 2012) : 138 sources, 7.8%
2800 GMRT population : 1526 sources with redshift and at least a multi-wavelength AGN diagnostic
MIPS 24 micron (RL AGN criterion) : 42 sources, 2.4%
BOSS AGN : 96 sources, 5.5%
Radio luminosity ($\log_{10} L_{1.4\,\mathrm{GHz}} \geq$ 25 WHz^{-1}) : 26 sources, 1.5%

Figure 9. A schematic of the various AGN selection.

down of classification from each indicator is illustrated in Figure 9, and Table 3 provides a matrix showing the correlation of classification among the different indicators. The most successful indicators, in terms of the number of objects identified as AGN, are the IRAC colours and BOSS spectral classification. We note that only one source from the Radio power AGN criterion out of a total of 26 sources, has an X-ray luminosity greater than 10^{42} erg s^{-1}. Also, two of these sources are confirmed as AGNs by the BOSS criterion whereas 6 of them are identified by the IRAC criterion. The

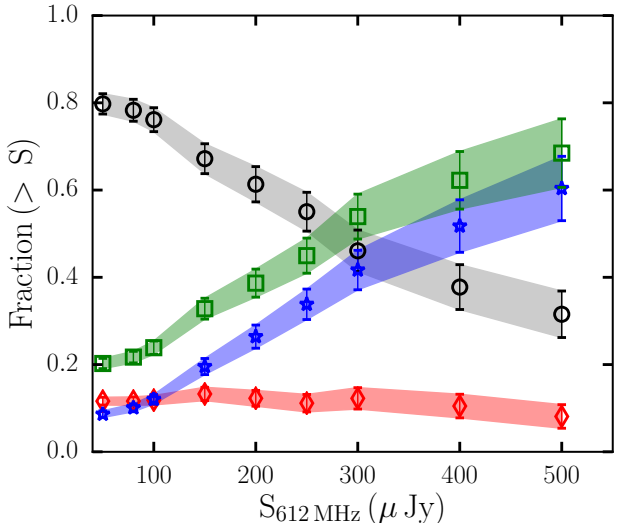

Figure 10. The relative fraction of AGN and SFG as a function of minimum flux density. The data points show the fraction of the sample greater than flux density, $S_{612\,\mathrm{MHz}}$, that are classified as RQ AGN (red diamonds), RL AGN (blue stars), all AGN (green squares) and SFG (black circles).

disagreement between the radio luminosity and the X-ray luminosity criterion may be attributed to heavily obscured sources in the X-rays, since radio observations are almost unaffected by dust extinction and therefore can detect even the most obscured systems (Del Moro et al. 2013).

We further classify the AGNs as RL AGN for all the sources with either $L_{1.4\,\mathrm{GHz}} > 10^{25}$ W Hz^{-1} (see Section 5.1) or $q_{24\mu\mathrm{m}}$ below the M82 locus (see Section 5.5). Above this threshold, a source is classified as a RQ AGN if it shows clear evidence of an AGN in the X-ray, in the BOSS/SDSS AGN spectroscopic classification, from its radio power or from its IRAC colors satisfying the Donley criterion. Table 4 presents the total number of AGNs and SFGs from a combination of the selection criteria for sources with redshifts. The objects classified as SFG are those sources in our redshift sample that do not show evidence of AGN activity in any of the diagnostics. This may be considered an upper limit to the population of sources in this flux density regime whose radio emission is powered by star formation processes. The large number of objects in our sample allows us to examine the change in population with flux density. Figure 10 shows the fraction of objects in each class in our sample as a function of limiting flux density. For a given flux density, $S_{612\,\mathrm{MHz}}$, the plot shows the fraction of objects that are classified as SFG, RL AGN, and RQ AGN in the sample of objects above that flux density. The green points shows the fraction for the total AGN population. The curves highlight the dramatic change in population over this flux density range. The SFG fraction exhibits a monotonic increase with decreasing flux density from ~30% to 80%. RL AGN decrease rapidly from being the dominant population above ~400 μJy to the smallest fraction below ~100 μJy. The fraction of RQ AGN remains roughly constant with flux density at ~10%.

Bonzini et al. (2013) found that ~ 60% of the 883 radio sources above ~ 50μJy from a VLA image at 1.4 GHz on ~ 0.3 deg^2 of the ECDFs to be SFGs, ~ 26% to be RQ

Table 3. Number of sources identified as AGN by each of the diagnostics. Entries indicate the number of AGN that are common to both indicators.

Indicator	Radio Luminosity	X-ray	BOSS AGN	IRAC colors	MIPS 24
Radio luminosity	26	-	-	-	-
X-ray	1	69	-	-	-
BOSS AGN	2	26	96	-	-
IRAC colors	6	35	45	138	-
MIPS 24	5	5	5	2	42

Table 4. Total number of SFGs, RQ AGNs and RL AGNs from a combination of the selection criteria for sources with redshift.

Class	Number	Fraction (%)
SFG	1226	80.3 %
RQ AGN	173	11.4 %
RL AGN	127	8.3 %

AGNs and ~ 14% to be RL AGNs. Rawlings et al. (2015) separated the same 1.4 GHz extragalactic radio source population as Bonzini et al. (2013) into AGN and SFGs by fitting IR SEDs constructed using IRAC, MIPS and SPIRE photometry. Overall, they found that for 40% of their sample the radio emission is powered by star formation, while for 20% of their sample the radio emission is powered by an AGN and the remaining 40% of their sample is made up by hybrids (i.e. no sign of jet activity, not clear whether or not the radio emission is powered by AGN).

Using a smaller but deeper 1.4 GHz sample reaching a 32.5 μJy flux limit over 0.29 deg^2 of the ECDFS VLA image, Padovani et al. (2015) identified 626 radio sources with redshifts and classified 55%, 25% and 20% as SFGs, RQ AGNs and RL AGNs respectively. Vernstrom et al. (2016) classified 10% RL AGN, 28% RQ AGN and 68% SFGs from 558 sources at 3 GHz in the Lockman Hole North from a single pointing with the JVLA.

For a spectral index of −0.7, the equivalent 1.4 GHz flux density threshold of our radio selected sample is 29 μJy, significantly deeper than the Bonzini et. al. study, and slightly deeper than Padovani et. al. The increased depth combined with our larger survey area provides a source sample that is 70% larger than the Bonzini study and over twice the size of the Padovani sample. In comparison to Bonzini et. al. our results indicate that the fraction of radio sources attributed to SFGs continues to increase rapidly with decreasing flux density, from ~60% to 80%. We also confirm that RQ AGN dominate over RL AGN, with 40% more RQ objects compared to RL objects in our sample.

We find a much higher fraction of SFG compared to the analysis of Padovani et. al., which found instead approximately equal fractions of SFG and AGN. This difference may be partially explained by the lower frequency of the GMRT sample, which selects against faint inverted spectrum sources, such as associated with compact AGN cores, that may be present in the VLA sample near the 1.4 GHz flux threshold. Future studies of the spectral index distribution of μJy radio sources will be important to resolve this difference.

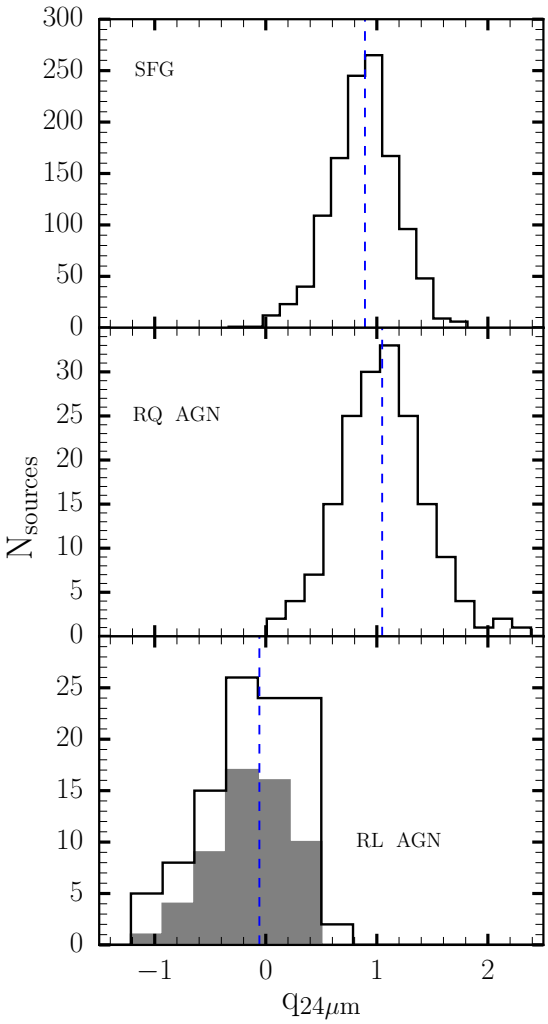

Figure 11. Distribution of the $q_{24\mu m}$-parameter for our selected SFG (top panel), RQ AGN (middle panel) and RL AGN (bottom panel). The shaded histogram in the bottom panel show the $q_{24\mu m}$ distribution for the RL AGNs selected from the upper limits given in equation 9 The dash vertical line in each panel designates the median value of the entire distribution, also listed in each panel.

6 DISCUSSION

6.1 Properties of the classified sources

The bottom panel of Figure 7 plots $q_{24\mu m}$ as a function of 1.4 GHz luminosity for SFGs (black stars), RQ AGNs (open red squares) and RL AGNs (open red circles). The $q_{24\mu m}$ parameter seems to show a decreasing trend with increasing

Table 5. Median values of redshift (z), $L_{1.4\,\mathrm{GHz}}$, $L_{\mathrm{IR}}/L_{\odot}$ and $< q_{24\mu\mathrm{m}} >$ for the different class of sources.

Class	$< z >$	$< \log_{10}(L_{1.4\,\mathrm{GHz}}) >$	$< \log_{10}(L_{\mathrm{IR}}/L_{\odot}) >$	$< q_{24\mu\mathrm{m}} >$
SFG	0.81 ± 0.01	23.24 ± 0.02	12.44 ± 0.04	0.89± 0.01
RQ AGN	1.09 ± 0.07	23.54 ± 0.07	12.61 ± 0.09	1.05± 0.03
RL AGN	0.88 ± 0.08	23.92 ± 0.13	13.02 ± 0.39	-0.06± 0.07

radio luminosity, and this is clearly evident for RL AGNs. In Figure 11 we show the distribution of $q_{24\mu\mathrm{m}}$for SFGs (top panel), RQ AGNs (middle panel) and RL AGNs (bottom panel). The median $q_{24\mu\mathrm{m}}$ value for SFGs is 0.89 ± 0.01 with a distribution that is peaked at the median with an RMS scatter of 0.18. The median $q_{24\mu\mathrm{m}}$ for RQ AGN is larger than for SFG at 1.05 ± 0.03 but like SFG is also peaked at the median with a slightly larger RMS of 0.24. RL AGN, on the other hand, have much lower median $q_{24\mu\mathrm{m}}$ of −0.06 ± 0.07, and a broader, less peaked distribution with a larger RMS scatter of 0.34.

Far-Infrared luminosities, L_{IR}, were derived from the integrated (8 - 1000μm, rest frame) far-infrared luminosities estimated by Rowan-Robinson et al. (2013) (RR13) using SWIRE photometry. We corrected the RR13 values to our more accurate spectroscopic redshift by

$$L_{\mathrm{IR}} = \frac{d_{\mathrm{L}}^2}{d_{\mathrm{L,RR13}}^2} L_{\mathrm{IR,RR13}}. \quad (10)$$

Here $\mathrm{d}_{\mathrm{L}}^2$ is the luminosity distance calculated using our redshift and $\mathrm{d}_{\mathrm{L,RR13}}^2$ is the luminosity distance using the RR13 redshifts.

The distributions of redshift, $L_{1.4\,\mathrm{GHz}}$ and FIR luminosities for the three populations are presented in Figure 12. The redshift distributions are shown in the left vertical panels. Photometric (empty) and spectroscopic (filled) redshift distributions are shown separately and grey shaded area indicates $z > 3$. We detect objects of all three types over the full redshift range up to $z > 3$. The median redshift for each is ∼1. Precise values are listed in Table 5.

The middle vertical panels of Figure 12 show the radio power distribution for the three class of sources . As for $q_{24\mu\mathrm{m}}$ SFG and RQ AGN show peaked distributions while the RL AGN have a wider distribution without a clear maximum. The distributions also show a consistent increase in the median radio power from SFG to RQ AGN to RL AGN. As shown in Table 5 the increase in the median is $\Delta(\log L_{1.4\mathrm{GHz}}) = 0.30 \pm 0.7$ between SFG and RQ AGN and $\Delta(\log L_{1.4\mathrm{GHz}}) = 0.38 \pm 0.15$ between RQ and RL AGN.

As shown in the right hand panel of Figure 12 and Table 5, the median L_{IR} and the width of the distributions increase from SFG, to RQ AGN and RL AGN. Figure 12 indicates the L_{IR} ranges corresponding to NIRGs, LIRGs, ULIRGs and HyLIRGs (see Patel et al. (2013)), and Table 6 shows the breakdown of the number of sources within each range for each class. The majority of the SFGs have L_{IR} in the range of LIRGS and ULIRGS. RQ AGNs are evenly distributed over LIRGs, ULIRGs and HyLIRGs, with very few in the NIRGS range. RL AGNs are more broadly distributed with the dominant faction at the low L_{IR} range.

6.2 The Far-Infrared Radio Correlation

We characterised the IR/radio properties of our sources by the logarithmic ratio between the IR bolometric (8-1000 μm) luminosity and the Radio 1.4 GHz luminosity q_{IR}(Helou et al. 1985):

$$q_{\mathrm{IR}} = \log_{10}\left(\frac{L_{\mathrm{IR}}}{3.75\times10^{12}\,\mathrm{W}}\right) - \log_{10}\left(\frac{L_{1.4\,\mathrm{GHz}}}{\mathrm{W\,Hz^{-1}}}\right) \quad (11)$$

Figure 13 presents radio power at 1.4 GHz versus FIR luminosity for SFGs detected by our classification. The contours represent the 1σ, 2σ and 3σ of the GMRT sources with radio and IR luminosity. The diagonal solid line in each panel show the q_{IR} relation given in equation 11 for the SFGs since the FIRC is believed to be driven mostly by star formation (Condon 1992; Yun et al. 2001). The dotted lines in all the panels indicate the ± 1σ dispersion in the value of the calculated q_{IR}. The SFGs have a tight FIRC, with a median q_{IR} value of 2.45 ± 0.01. The selected RQ AGNs also show a tight correlation in agreement with the FIRC, with a median q_{IR} value of 2.47 ± 0.04. RL AGNs lie well above the FIRC for SFGs and RQ AGNs with a median q_{IR} value of 1.43 ± 0.07. This difference for RL AGNs can be attributed to the additional AGN component to radio emission (Rawlings et al. 2015).

Our median q_{IR} = 2.45 ± 0.01 for SFG is in good agreement with a measurement, e.g. Ivison et al. (2010)), who used submillimetre galaxy (SMG) samples with radio emission to measure a median q_{IR} = 2.40 ± 0.2 for a sample of IR-bright ($S_{250\mu\mathrm{m}} \gtrsim 20$ mJy) galaxies out to $z < 3.5$. Our median q_{IR} is higher, however, than the value of q_{IR} = 2.17±0.1, as measured by Magnelli et al. (2010) for a sample of bright ($S_{850\mu\mathrm{m}} > 5$ mJy) single-dish submillimetre sources observed in GOODS-N, and lower than that reported by Thomson et al. (2014), who measured a median q_{IR} = 2.56 ± 0.05 for 870 μm-selected submillimetre galaxies, observed at high resolution with ALMA in the Extended Chandra Deep Field South. Our measurement of q_{IR} is also lower than that reported by Bell (2003) who measured q_{IR} = 2.64 ± 0.02 for 162 galaxies with IR and radio data and no signs of AGN by assembling a sample of SFGs with FUV, IR and radio data to quantitatively explore the radio-IR correlation. Our value of q_{IR} from a larger low-frequency selected sample lies thus within the range of variation of values derived from submillimetre selected samples.

6.3 Radio emission in SFGs and RQ AGNs

Miller et al. (1993) suggested that RQ AGNs are a scaled-down version of RL AGNs at lower radio power whilst Sopp & Alexander (1991) found that the major contribution to the radio emission in these system is due to the star formation in the host galaxy. However, the study of the cosmological

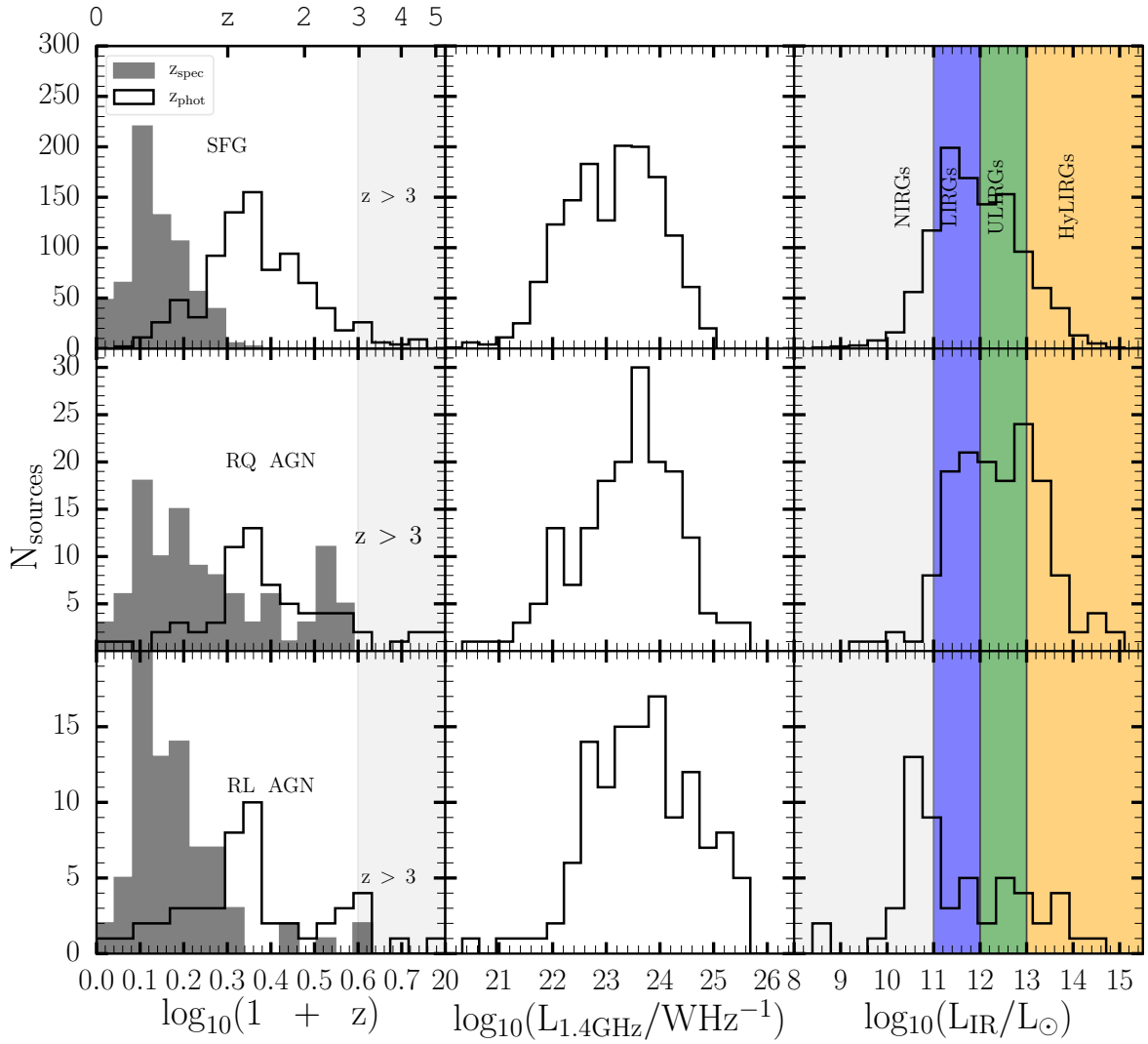

Figure 12. Distribution of SFG (top panels), RQ AGN (middle panels) and RL AGN (bottom panels) for their redshifts, $L_{1.4\ GHz}$ and FIR luminosities respectively. The left vertical panels represent the distributions for spectrocopic (filled) and photometric (empty) redshifts for the various class of sources. The grey shaded areas show $z > 3$. The middle vertical panels represent the radio power distributions. The limits of NIRGs, LIRGs, ULIRGs and HyLIRGs (Patel et al. 2013) are shown as grey, blue, green and orange shaded areas respectively in the right vertical panels to represent the range of sources based on their FIR luminosity.

Table 6. Number of NIRGs, LIRGs, ULIRGs and HyLIRGs in the subsample according to their star-forming, radio-quiet and radio-loud FIR luminosities.

$\log_{10}(L_{IR}/L_{\odot})$ range	Type	SFG#	RQ AGN#	RL AGN#
≤ 11	NIRG	149	11	23
11 – 12	LIRG	439	45	14
12 – 13	ULIRG	339	48	8
≥ 13	HyLIRG	155	45	10

evolution and luminosity function by Padovani et al. (2011), found that their radio emissions are significantly different for the two types of AGNs, while they are indistinguishable for SFGs and RQ AGNs. We characterize nature of the radio emission from the three types by comparing the star formation rates inferred from the IR and radio. The empirical conversion between the radio power at 1.4 GHz and the SFR of the galaxy according to (Murphy et al. 2011) is:

$$SFR_{radio}[M_{\odot}\,yr^{-1}] = \log_{10}(L_{1.4\,GHz}) - 21.20 \quad (12)$$

In Figure 14 we compare the SFR computed from the FIR luminosities by Rowan-Robinson et al. (2013) with the SFR derived from the radio luminosities for our classified SFGs

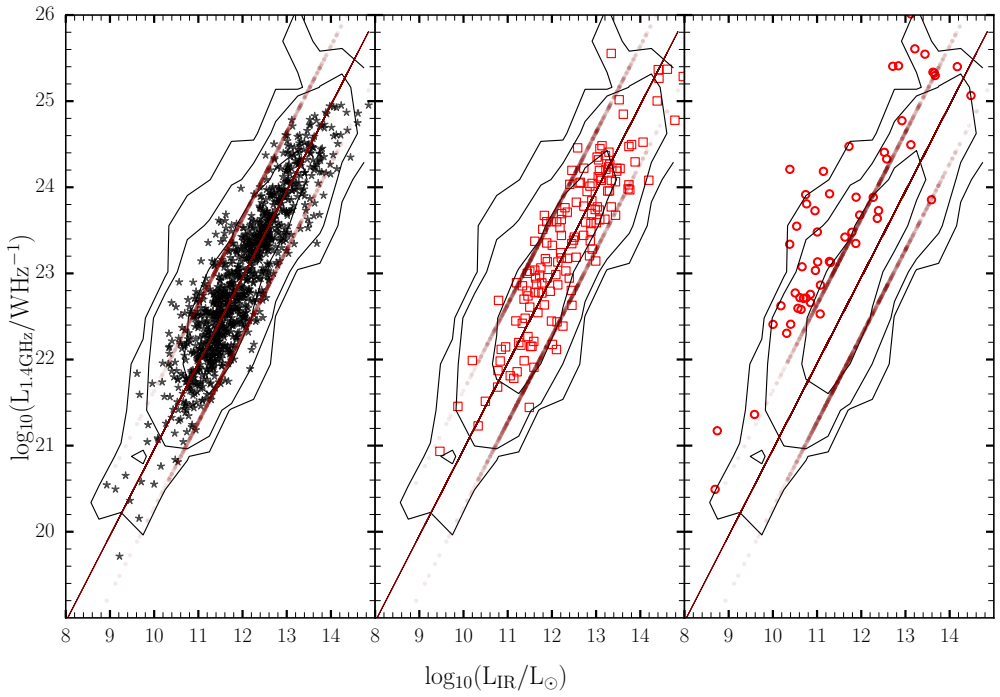

Figure 13. $\log_{10}(L_{1.4\,\mathrm{GHz}})$ versus $\log_{10}(L_{\mathrm{IR}}/L_{\odot})$ for SFG (first panel), RQ AGN (middle panel) and RL AGN (last panel) according to the AGN selection described in Section 5.6. The contours show 1σ, 2σ and 3σ confidence intervals of the GMRT sources with radio and IR luminosity respectively. The diagonal solid line in each panel show the q_{IR} relation given in equation 11 for the SFGs.

and RQ AGN. A regression fit to the data yields:

$$\log_{10}(\mathrm{SFR_{FIR}}) = 0.95 \pm 0.02 \times \log_{10}(\mathrm{SFR_{radio}}) - 0.02 \pm 0.03 \quad (13)$$

for all the sources with redshifts having infrared and radio luminosities, while for SFG alone we obtain

$$\log_{10}(\mathrm{SFR_{FIR}})_{\mathrm{SFG}} = 0.98 \pm 0.02 \times \log_{10}(\mathrm{SFR_{radio}})_{\mathrm{SFG}} - 0.07 \pm 0.03 \quad (14)$$

and for RQ AGN

$$\log_{10}(\mathrm{SFR_{FIR}})_{\mathrm{RQ\,AGN}} = 1.04 \pm 0.05 \times \log_{10}(\mathrm{SFR_{radio}})_{\mathrm{RQ\,AGN}} - 0.12 \pm 0.11 \quad (15)$$

The fits for the SFGs and RQ AGNs (shown as black and red lines respectively in Figure 14), are not significantly different within errors, suggesting that the main contribution to the radio emission in RQ AGN is due to the star formation in the host galaxy rather than black hole activity. Thus radio power is a good tracer for the SFR also in RQ AGNs.

6.4 Star forming galaxies at high redshift

The SFG in our radio sample, while predominantly at z < 2, include some objects with photometric redshifts much larger, including 27 sources with $z \geq 3$. We investigate the reliability of such high redshifts by following the analysis of Wang et al. (2012), who presented a new color selection of extremely red objects (EROs) (i.e. most extreme dust-hidden high-redshift galaxies) with K_S and IRAC colors of $K_S - 4.5\mu\mathrm{m} > 1.6$. The photometric redshifts used by Wang et al. (2012) to select EROs are between 1.5 and 5, with ~70% at $z \sim 2-4$. This selection aims at galaxies at $z > 2$ whose extremely red colors are likely caused by large dust extinction. We use their approach to examine our SFGs sample and in particular where our objects at $z > 3$ reside in the diagnostic plot. Figure 15 presents the K_S, 3.6 and 4.5 color-color diagram for our selected SFGs color coded according to redshift (top panel) and, also the same sample with the same redshift demarcations used by Wang et al. (2012). The top panel shows that SFGs at high redshifts have $2.5\log_{10}(S_{4.5}/S_{K_S}) > 0$, consistent with this high redshift selection criterion.

7 CONCLUSION

This work was aimed at disentangling the different radio populations that contribute to the faint radio sky. We have explored different AGN indicators from the radio, mid-infrared, optical and X-ray. We reaffirm that the ratio between the mid-infrared and radio flux parametrised by the $q_{24\mu m}$ value, demonstrated in Bonzini et al. (2013), is an important parameter to identify RL AGNs. Our scheme expands on the one adopted by Bonzini et al. (2013) and combines radio, mid-infrared, optical and X-ray data to efficiently separate the radio source population with redshift associations into three classes: SFGs, RQ AGNs and RL AGNs.

We have determined the relative contribution of the three classes of sources to the subsample of 1526 radio sources with redshifts and at least one multi-wavelength diagnostic and find that ~80% are SFGs, ~12% are RQ AGNs

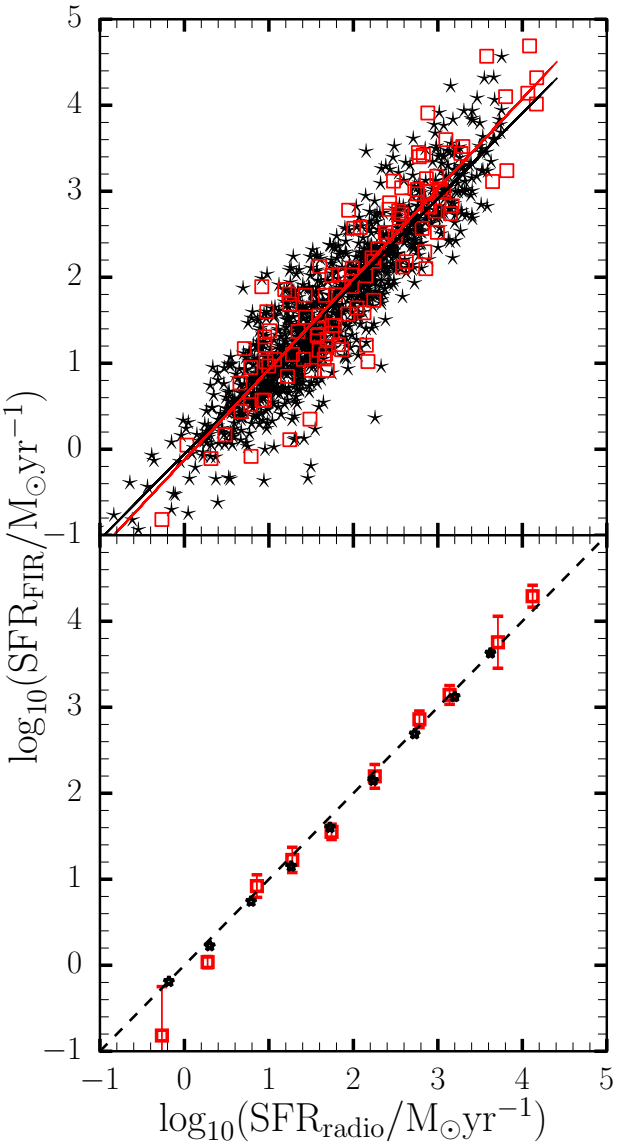

Figure 14. SFR derived from the FIR luminosity versus the SFR from the radio luminosity. SFGs are plotted as black stars and RQ AGNs as open red squares. The bottom panel show the binned $\log_{10}$(SFR) for the SFGs and the RQ AGNs in bin width of 0.5$\log_{10}$(SFR)

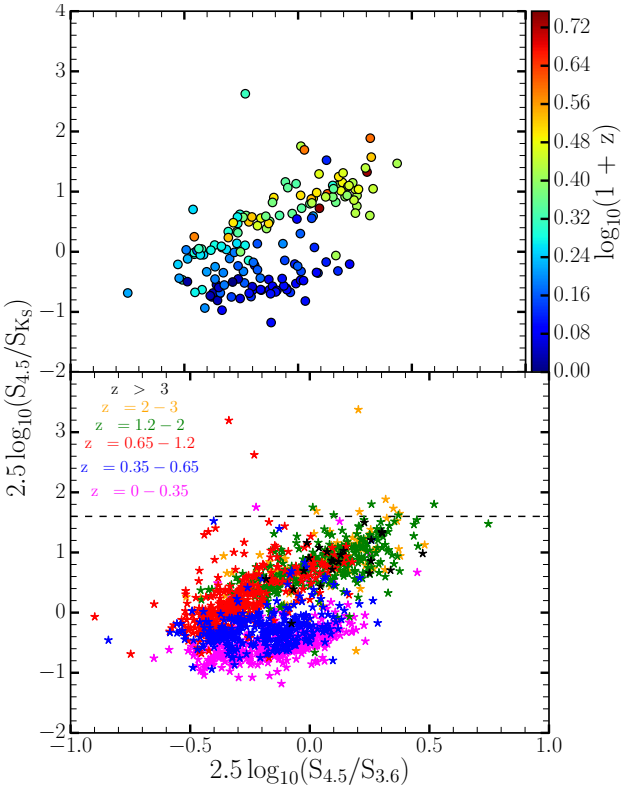

Figure 15. K_s, 3.6 and 4.5 color-color diagram. Top panel: SFGs color coded with redshift. Bottom panel: SFG sources with same redshift demarcation ranges following (Wang et al. 2012).

and ~8% are RL AGNs. Compared to previous analysis of sources over smaller areas at 1.4 GHz in the ECDFS, our result indicates a continued increase in the relative fraction of SFG with decreasing flux density, and confirm that RQ objects dominate the AGN population. The significantly higher fraction of SFG in our sample may also partially arise from the selection at lower frequency, where at a given flux density threshold flat-spectrum AGN cores are preferentially detected at 1.4 GHz. Multi-frequency investigations to explore the spectral index distribution of μJy radio sources will help resolve this question.

The median redshift of our radio sources for all three categories is ~1, although in all cases detections span the entire range up to $z > 3$. The median values of both the radio and infrared luminosity systematically increases from SFG, to RQ AGN and RL AGN (see Table 5).

The median $q_{24\mu m}$ for SFG, 0.89 ± 0.01 is slightly below that for RQ AGN, 1.05 ± 0.03, but both differ substantially from the value for RL AGN of -0.06 ± 0.07. In contrast to $q_{24\mu m}$, SFG and RQ AGN show no difference in the ratio of radio to bolometric IR luminosity, with $q_{\rm IR}$ of of 2.45 ± 0.01 and 2.47 ± 0.04 respectively. The Far-IR Radio correlation ($q_{\rm IR}$) seen in the SFGs is in good agreement with the value found locally (Yun & Carilli 2002) and at higher redshift (Ivison et al. 2010; Seymour et al. 2011). Although the median radio luminosity of the RQ AGN population is slightly higher than the SFGs, there is no distinction between the objects in Far-IR radio correlation, suggesting that the radio emission from RQ AGN host galaxies results primarily from star formation activity. The RL AGN on the other hand are systematically above the Far-IR correlation for SFG and RQ AGN, with a median $q_{\rm IR}$ of 1.54 ± 0.06, indicating the presence of additional AGN-powered radio emission.

The need to better understand the faint radio source population in the high redshift universe is one of the key motivation for the construction of the next generation of very large radio telescopes such as the SKA. In this study we presented an multi-wavelength analysis to classify the μJy population. It is clear that SFG will form a high and growing fraction of the radio sources as we probe deeper. Next-generation surveys will thus probe beyond the AGN phenomenon to the underlying radio astrophysics of the evolution of galaxies and star formation. The GMRT data pre-

sented here in total intensity also includes full-Stokes polarimetry. An exploration of the polarisation properties of this faint radio source population will be the subject of a subsequent paper.

ACKNOWLEDGEMENTS

The authors acknowledge support from the Square Kilometre Array South Africa project, the South African National Research Foundation and Department of Science and Technology. E.F.O. acknowledges funding from the National Astrophysics and Space Science Programme. MV acknowledges support from the European Commission Research Executive Agency (FP7-SPACE-2013-1 GA 607254), the South African Department of Science and Technology (DST/CON 0134/2014) and the Italian Ministry for Foreign Affairs and International Cooperation (PGR GA ZA14GR02).

We thank the staff of the GMRT that made these observations possible. GMRT is run by the National Centre for Radio Astrophysics of the Tata Institute of Fundamental Research.

This work is based in part on observations made with the *Spitzer Space Telescope*, which is operated by the Jet Propulsion Laboratory, California Institute of Technology under a contract with NASA.

REFERENCES

Alam S., et al., 2015, ApJS, 219, 12
Appleton P. N., et al., 2004, ApJS, 154, 147
Bell E. F., 2003, ApJ, 586, 794
Bolton A. S., et al., 2012, AJ, 144, 144
Bonzini M., Padovani P., Mainieri V., Kellermann K. I., Miller N., Rosati P., Tozzi P., Vattakunnel S., 2013, MNRAS, 436, 3759
Brammer G. B., van Dokkum P. G., Coppi P., 2008, ApJ, 686, 1503
Cardamone C. N., et al., 2010, ApJS, 189, 270
Casey C. M., Chapman S. C., Muxlow T. W. B., Beswick R. J., Alexander D. M., Conselice C. J., 2009, MNRAS, 395, 1249
Cole S., et al., 2005, MNRAS, 362, 505
Condon J. J., 1992, ARA&A, 30, 575
Cutri R. M., et al., 2003, VizieR Online Data Catalog, 2246
Dadina M., 2008, A&A, 485, 417
Del Moro A., Alexander D. M., Mullaney J. R., Daddi E., Bauer F. E., Pope A., 2013, Mem. Soc. Astron. Italiana, 84, 665
Donley J. L., et al., 2012, ApJ, 748, 142
Eisenstein D. J., et al., 2005, ApJ, 633, 560
Eisenstein D. J., et al., 2011, AJ, 142, 72
Fadda D., Rodighiero G., 2014, MNRAS, 444, L95
Garn T., Alexander P., 2008, Monthly Notices of the Royal Astronomical Society, 391, 1000
Garn T., Alexander P., 2009, MNRAS, 394, 105
Garn T., Green D. A., Riley J. M., Alexander P., 2008, Monthly Notices of the Royal Astronomical Society, 383, 75
Gebhardt K., et al., 2000, ApJ, 539, L13
Georgakakis A., Nandra K., Laird E. S., Aird J., Trichas M., 2008, MNRAS, 388, 1205
Giroletti M., Panessa F., 2009, ApJ, 706, L260
González-Solares E. A., et al., 2011, MNRAS, 416, 927
Grant J. K., et al., 2010, The Astrophysical Journal, 714, 1689
Griffin M. J., et al., 2010, A&A, 518, L3
Helou G., Soifer B. T., Rowan-Robinson M., 1985, ApJ, 298, L7
Hernán-Caballero A., et al., 2009, MNRAS, 395, 1695
Hurley P. D., et al., 2017, MNRAS, 464, 885
Huynh M. T., Gawiser E., Marchesini D., Brammer G., Guaita L., 2010, ApJ, 723, 1110
Ibar E., Ivison R. J., Best P. N., Coppin K., Pope A., Smail I., Dunlop J. S., 2010, MNRAS, 401, L53
Ilbert O., et al., 2009, ApJ, 690, 1236
Ivison R. J., et al., 2010, A&A, 518, L31
Jiang L., Fan X., Ivezić Ž., Richards G. T., Schneider D. P., Strauss M. A., Kelly B. C., 2007, ApJ, 656, 680
Kimball A. E., Kellermann K. I., Condon J. J., Ivezić Ž., Perley R. A., 2011, ApJ, 739, L29
Kormendy J., Bender R., Evans A. S., Richstone D., 1998, AJ, 115, 1823
Lacy M., et al., 2004, ApJS, 154, 166
Lacy M., Sajina A., Petric A. O., Seymour N., Canalizo G., Ridgway S. E., Armus L., Storrie-Lombardi L. J., 2007, ApJ, 669, L61
Laird E. S., et al., 2009, ApJS, 180, 102
Lang D., Hogg D. W., Schlegel D. J., 2016, AJ, 151, 36
Lawrence A., et al., 2007, MNRAS, 379, 1599
Lonsdale C. J., et al., 2003, PASP, 115, 897
Luchsinger K. M., et al., 2015, AJ, 150, 87
Magnelli B., et al., 2010, A&A, 518, L28
Manners J. C., et al., 2003, MNRAS, 343, 293
Mauch T., Sadler E. M., 2007, MNRAS, 375, 931
Mauduit J.-C., et al., 2012, PASP, 124, 714
McLure R. J., Dunlop J. S., 2002, MNRAS, 331, 795
Miller P., Rawlings S., Saunders R., 1993, MNRAS, 263, 425
Murphy E. J., et al., 2011, ApJ, 737, 67
Norris R. P., et al., 2006, AJ, 132, 2409
Padovani P., Mainieri V., Tozzi P., Kellermann K. I., Fomalont E. B., Miller N., Rosati P., Shaver P., 2009, ApJ, 694, 235
Padovani P., Miller N., Kellermann K. I., Mainieri V., Rosati P., Tozzi P., 2011, ApJ, 740, 20
Padovani P., Bonzini M., Kellermann K. I., Miller N., Mainieri V., Tozzi P., 2015, MNRAS, 452, 1263
Patel H., Clements D. L., Vaccari M., Mortlock D. J., Rowan-Robinson M., Pérez-Fournon I., Afonso-Luis A., 2013, MNRAS, 428, 291
Prandoni I., Gregorini L., Parma P., de Ruiter H. R., Vettolani G., Wieringa M. H., Ekers R. D., 2001, A&A, 365, 392
Rawlings J. I., et al., 2015, MNRAS, 452, 4111
Rieke G. H., et al., 2004, ApJS, 154, 25
Rousseeuw P. J., Croux C., 1993, Journal of the American Statistical Association, 88, 1273
Rowan-Robinson M., et al., 2008, MNRAS, 386, 697
Rowan-Robinson M., Gonzalez-Solares E., Vaccari M., Marchetti L., 2013, MNRAS, 428, 1958
Rowan-Robinson M., et al., 2016, MNRAS, 461, 1100
Sajina A., Yan L., Lacy M., Huynh M., 2007, ApJ, 667, L17
Sajina A., et al., 2008, ApJ, 683, 659
Sargent M. T., et al., 2010, ApJ, 714, L190
Serjeant S., et al., 2004, MNRAS, 355, 813
Seymour N., et al., 2008, MNRAS, 386, 1695
Seymour N., et al., 2011, MNRAS, 413, 1777
Sopp H. M., Alexander P., 1991, MNRAS, 251, 112
Stern D., et al., 2005, ApJ, 631, 163
Szokoly G. P., et al., 2004, ApJS, 155, 271
Taylor A. R., Jagannathan P., 2016, MNRAS, 459, L36
Taylor E. N., et al., 2009, ApJS, 183, 295
Thomson A. P., et al., 2014, MNRAS, 442, 577
Tremaine S., et al., 2002, ApJ, 574, 740
Trichas M., Georgakakis A., Rowan-Robinson M., Nandra K., Clements D., Vaccari M., 2009, MNRAS, 399, 663
Vaccari M., 2015, in The Many Facets of Extragalactic Radio Surveys: Towards New Scientific Challenges. p. 27 (arXiv:1604.02353)
Vaccari M., 2016, The Universe of Digital Sky Surveys, 42, 71

Vaccari M., et al., 2010, A&A, 518, L20
Vernstrom T., Scott D., Wall J. V., Condon J. J., Cotton W. D., Kellermann K. I., Perley R. A., 2016, MNRAS, 462, 2934
Vito F., Gilli R., Vignali C., Comastri A., Brusa M., Cappelluti N., Iwasawa K., 2014, MNRAS, 445, 3557
Wang W.-H., Barger A. J., Cowie L. L., 2012, ApJ, 744, 155
York D. G., et al., 2000, AJ, 120, 1579
Yun M. S., Carilli C. L., 2002, ApJ, 568, 88
Yun M. S., Reddy N. A., Condon J. J., 2001, ApJ, 554, 803

This paper has been typeset from a TEX/LATEX file prepared by the author.